

AERODYNAMIC OPTIMISATION OF BIOINSPIRED CORRUGATED WINGS FOR HIGH-EFFICIENCY MAV GLIDING

Melos Krasniqi[1] & Sophie F. Armanini[2]

[1,2]Imperial College London, Department of Aeronautics, South Kensington, London SW7 2AZ, United Kingdom
Email: [1] melos_krasniqi@outlook.com / [2] s.armanini@imperial.ac.uk
Tel: [2] +44 (0)20 7594 3511

Abstract

Micro air vehicles operate at low Reynolds numbers where conventional smooth lifting surfaces are prone to laminar separation, early stall, and poor lift-to-drag performance. This study investigates whether dragonfly-inspired wing corrugation can improve gliding efficiency for a tandem-wing MAV-scale glider. Eighteen configurations with varying planform, corrugation waveform, corrugation amplitude, and chordwise corrugation location were manufactured and tested in free flight using an elastic launcher and VICON motion capture system. Results show that the best gliding performance was achieved using a rectangular planform with low-amplitude sinusoidal corrugation confined to the trailing-edge region, producing an approximately 17.5% increase in effective L/D relative to the smooth rectangular baseline at $Re \approx 9 \times 10^3$. Corrugation location was the dominant factor affecting glide performance, accounting for approximately 46% of the one-way main-effect contribution in the screening analysis, followed by amplitude at approximately 40%, while planform and waveform each contributed less than 10%. Two-dimensional implicit unsteady CFD simulations of the smooth baseline and best-performing corrugated case were then performed to interpret the flow physics. The simulations indicate that trailing-edge corrugation promotes valley-trapped vortices, forms an effective pseudo-aerofoil contour, and produces a cleaner forewing wake that improves the hindwing operating environment. The results suggest that low-amplitude trailing-edge corrugation offers a practical design feature for improving MAV gliding efficiency.

Keywords: MAVs, Corrugation, Low-Reynolds Aerodynamics, Tandem Wings, Bioinspired Flight

https://doi.org/10.71945/icas2026_0665

1. Introduction

The process of biomimicry has been used by engineers throughout history, especially in the field of aerodynamics. Micro air vehicles (MAVs) are small, remotely piloted or autonomous aircraft designed for missions where compact size, low cost, and access to confined environments are required. Their use is becoming increasingly widespread across industries, including inspection, monitoring, and environmental tracking. However, they are limited in endurance and range by restricted onboard energy storage. This is especially true for multi-rotor MAVs, which possess hovering capability and high manoeuvrability, but must continuously expend power to remain airborne. Fixed-wing MAVs, however, can exploit the advantages of wing-borne flight, and even passive methods such as gliding.

The benefit of fixed-wing gliding is, however, limited by the low-Re regime in which MAVs operate. At these scales, viscous effects, laminar separation bubbles, and early stall limit aerodynamic efficiency for conventional wing geometries [1, 2, 3]. This motivates the study of biological flyers, which, despite these challenges, exhibit efficient gliding properties.

Dragonflies are one of the few insect species known to use gliding flight, combining this efficient flight mode with extreme manoeuvrability and a low acoustic signature [4]. Given their tandem-wing configuration, they also present the opportunity to exploit interactive aerodynamic effects between the forewing and hindwing pairs to optimise gliding efficiency. Dragonflies also exhibit structural and aerodynamic traits that directly support gliding. Their high aspect ratio (AR) wings reduce induced drag, whilst corrugation patterns stiffen the membrane [5] and help to generate vortices in the grooves [6], enabling the wings to sustain lift during extended glides.

Dragonfly aerodynamics have been studied in-depth using computational fluid dynamics (CFD) [7, 8, 9]. Whilst this provides a useful understanding of aerodynamic interactions, CFD studies inherently depend on ideal assumptions, with uncertainties arising from manufacturing imperfections and atmospheric variability. In addition, wind tunnel investigations [10, 11], and particle image velocimetry (PIV) [12, 13] studies have been conducted. These also lay important groundwork in understanding flow structures and validating computational models, especially since they take into consideration real-world manufacturing errors when models are created. However, they remain constrained by artificial testing environments. In wind tunnels, models are typically mounted in fixed or semi-fixed configurations. This means that whilst steady aerodynamic parameters can be measured, fully unconstrained six-degree-of-freedom (6-DOF) free-flight behaviour is not generally replicated [14].

A remaining research gap is therefore a lack of systematic free-flight data that shows how corrugation pattern, amplitude, location, and planform shape affect the gliding performance of a tandem-wing MAV-scale vehicle. This study addresses that gap by testing eighteen configurations using a repeatable free-flight methodology with VICON motion capture. The objective is to identify the dominant geometric variables affecting aerodynamic efficiency and use implicit unsteady CFD to interpret the flow mechanisms responsible for the observed differences in performance.

This work forms part of a wider study on the optimisation of tandem-wing gliding MAVs, where the performance of the forewings and hindwings cannot be considered entirely independently. The use of a tandem-wing setup means that the measured performance includes the direct aerodynamic effects of varying the parameters, as well as the indirect influence of the forewing wake interaction on the hindwing. Thus, this research provides design guidance for low-Reynolds tandem-wing gliders, whilst also yielding insight into mechanisms that are relevant to single-wing MAVs as well.

2. Methodology

The methodology consisted of four key stages: selecting the geometric parameters, defining a reduced test matrix, manufacturing the physical prototypes, and measuring glide performance during free-flight. The resulting trajectories were used to compute glide angles and $\left(\frac{L}{D}\right)_{\text{eff}}$, which served as the primary performance metrics.

Four design variables were considered: corrugation type, corrugation amplitude, corrugation location, and wing planform shape. The selected factor levels are summarised in Table 1, with the amplitude and location definitions given in Tables 2 and 3, respectively.

Table 1 – Design variables and factor levels used in the experimental campaign.

Parameter	**Option 1**	**Option 2**	**Option 3**
Wing planform shape	Bio-inspired	Rectangular	–
Corrugation type	Sinusoidal	Triangular	Bio-inspired
Corrugation amplitude	Low amplitude	Medium amplitude	High amplitude
Corrugation location	Leading edge	Trailing edge	Full chord

Three corrugation types were considered: bio-inspired, sinusoidal, and triangular. The bio-inspired pattern was based on the mid-span corrugation of *Aeshna cyanea*, which is commonly used in dragonfly corrugation studies [10]. The triangular pattern was used to compare against a regular non-tapering sharp-peak geometry, similar to the approach used by Meng and Sun [15]. The sinusoidal pattern was used to analyse the effect of a smoother corrugation peak and was defined as,

$$y(x) = \frac{A}{2}\sin\left(\frac{2\pi(x-x_1)}{\lambda}\right), \qquad x_1 \leq x \leq x_2 \tag{1}$$

where $y(x)$ is the vertical displacement at chordwise position x, A is the peak-to-trough corrugation height, λ is the wavelength, and $x_1 \leq x \leq x_2$ defines the chordwise interval over which the corrugation is applied.

Corrugation amplitude was varied across three levels: low, medium, and high. The peak-to-trough height of the corrugation was defined as a percentage of the MAC. Whilst there is no convention for defining this amplitude, the range of corrugation amplitudes in existing research ranges from 3% to 6% [16]. For this reason, the increments set out in Table 2 were chosen.

Table 2 – Definition of corrugation amplitude levels as a percentage of MAC

Level	**Corrugation Amplitude (% of MAC)**
Low	2%
Medium	4%
High	6%

Corrugation location was varied across three chordwise regions: leading-edge (LE), trailing-edge (TE), and full chord. The LE range follows Meng and Sun [17], with the TE range applied symmetrically aft and shown in Table 3, where c denotes the MAC.

Table 3 – Definition of corrugation locations as a function of chord length

Location	**Chordwise Range (x/c)**
Leading edge	$0.0 \leq x/c \leq 0.6$
Trailing edge	$0.4 \leq x/c \leq 1.0$
Full chord	$0.0 \leq x/c \leq 1.0$

A full factorial study of the three 3-level factors and one 2-level factor would require 54 corrugated configurations, excluding smooth baselines. To reduce the experimental burden while retaining main-effect estimates, a modified L18 screening matrix based on Taguchi principles was used [18, 19].

This provided 18 configurations, including smooth baselines, shown in Table 4.

Table 4 – Modified L18 screening matrix for dragonfly-inspired wing testing

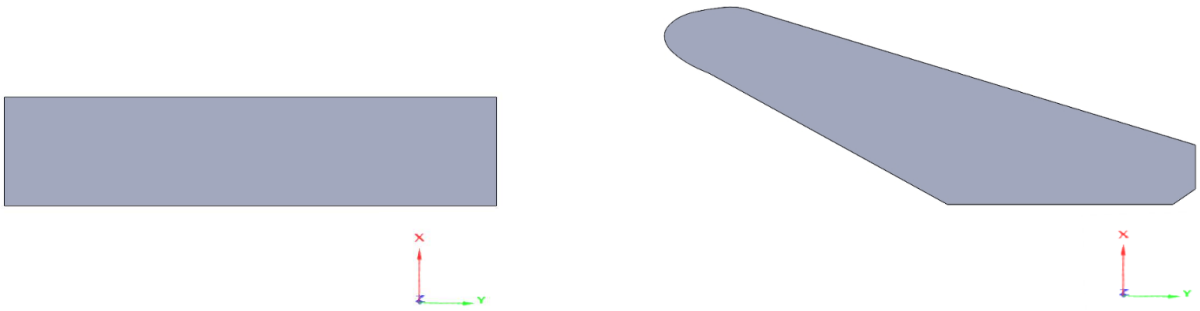
Run	Planform	Corrugation Type	Amplitude	Location
1	Rectangular	Smooth	NA	NA
2	Rectangular	Triangular	High	Leading edge
3	Rectangular	Triangular	Low	Leading edge
4	Rectangular	Sinusoidal	Medium	Full chord
5	Rectangular	Sinusoidal	Low	Trailing edge
6	Rectangular	Bio-inspired	High	Trailing edge
7	Rectangular	Triangular	High	Full chord
8	Rectangular	Bio-inspired	Low	Leading edge
9	Rectangular	Sinusoidal	High	Trailing edge
10	Bio-inspired	Smooth	NA	NA
11	Bio-inspired	Triangular	Medium	Leading edge
12	Bio-inspired	Sinusoidal	High	Leading edge
13	Bio-inspired	Bio-inspired	Medium	Leading edge
14	Bio-inspired	Bio-inspired	Low	Full chord
15	Bio-inspired	Sinusoidal	Medium	Trailing edge
16	Bio-inspired	Triangular	Medium	Full chord
17	Bio-inspired	Bio-inspired	Medium	Full chord
18	Bio-inspired	Sinusoidal	Low	Leading edge

2.1 Wing Design Parameters

The wing design variables are defined below. Chordwise locations are reported using x/c, where c is the mean aerodynamic chord (MAC). The bio-inspired planform was based on the Giant Petaltail (*Petalura ingentissima*), selected for its gliding capability and reconstructed from an open-source scaled reference image [20]. The geometry was scaled by a factor of two for the glider design. To enable fair comparison, the rectangular and bio-inspired wings were matched in planform area, MAC, thickness, and Reynolds number. The final dimensions are shown in Table 5, with the planforms shown in Figure 1.

Table 5 – Geometric parameters of the rectangular and bio-inspired wings.

Parameter	Rectangular wing	Bio-inspired wing
Planform area S [mm^2]	3395	3395
Mean aerodynamic chord (MAC) [mm]	27.4	27.4
Wing thickness [mm]	0.8	0.8



(a) Rectangular wing

(b) Bio-inspired wing

Figure 1 – Comparison of wing planforms used in this study: (a) rectangular and (b) bio-inspired.

The microglider models were manufactured using fused deposition modelling (FDM). Lightweight-PLA (LW-PLA) was used for the wings, nose, and tailplane to reduce mass, while standard PLA was used for the wing mounts to preserve dimensional accuracy. A carbon-fibre square rod formed the fuselage. The nose was ballasted to provide greater stability in flight. All configurations were ballasted to the same total mass before testing (Table 6). This also ensured that the centre of gravity (CoG) was at 150 mm aft of the nose ($\frac{x_{\mathrm{CoG}}}{L} \approx 0.60$, where L is the total length of the glider).

Table 6 – Component masses

Component	**Mass (g)**
Nose assembly including ballast	1.23
Tail	0.47
Fuselage	3.00
Wings + Mounts + Ballast	10.77
Total	15.47

All wings were mounted at a wing incidence angle of 4°, with zero decalage between the fore- and hindwing. The wing pairs were separated by $1.5c$ horizontally and $0.2c$ vertically, following stable tandem-wing configurations reported in literature [21]. The longitudinal wing position was adjusted during preliminary launches to obtain stable glides for each planform, and found to be $\frac{x}{L} \approx 0.62$ for the forewing and $\frac{x}{L} \approx 0.79$ for the hindwing, measured from the nose tip to the root leading edge. An example glider model is shown in Figure 2.

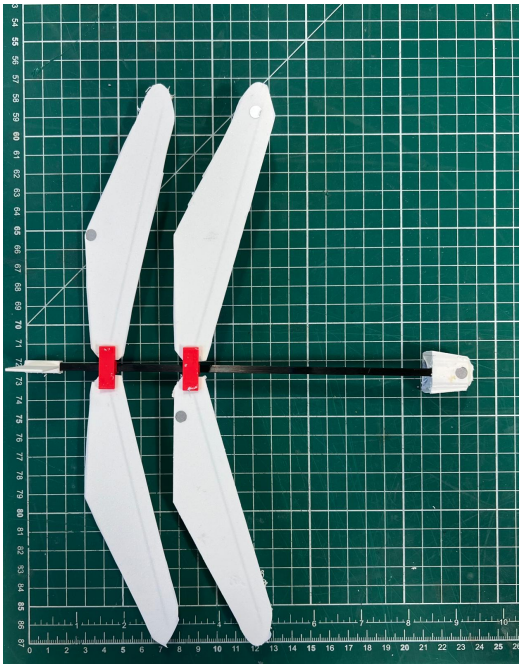
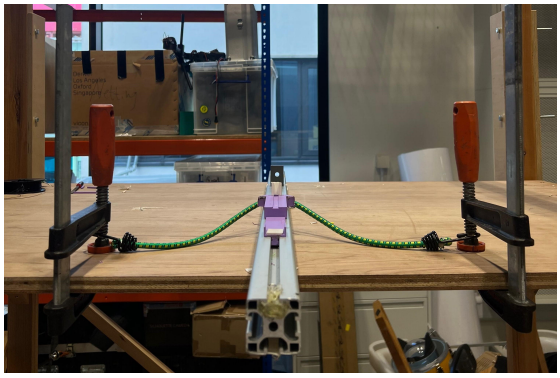


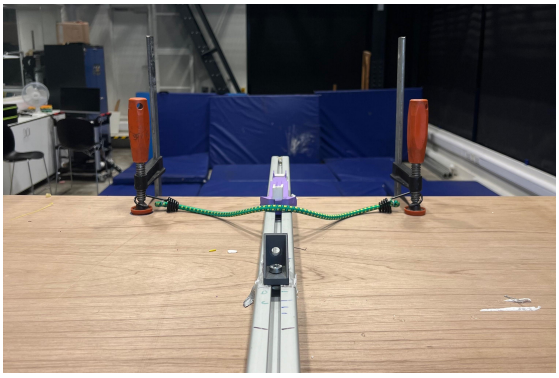
Figure 2 – Example assembled glider configuration used in the flight-test campaign.

2.2 Flight Testing

The tests were conducted in the Brahmal Vasudevan Multi Terrain Aerial Robotics Arena at Imperial College London, which provided a $10 \times 6.2 \times 5.5$ m indoor flight volume equipped with 16 VICON T40 cameras [22]. This setup provided sufficient clearance for repeated launches while allowing the prototype motion to be tracked consistently throughout the glide. The launcher used for the flight-test campaign is shown in Figure 3. The launcher was operated by placing the glider on a 3D-printed coupler, which was pulled against a bungee cord up to a back-stop. The bungee cord was then released, accelerating the glider along the rail until it hit a front-stop, thus launching the glider.



(a) Front view of the final launcher with front-stop



(b) Rear view of the final launcher with back-stop

Figure 3 – Launcher used for the flight-test campaign.

A VICON motion capture system was used to track 6 mm retro-reflective markers attached to the gliders. Recording began immediately before release of each prototype from the launcher. Each model was weighed before launch to ensure equal mass across tests. A glide was deemed valid if all markers remained visible except brief recoverable occlusions (less than 10 frames) in flight. Each configuration was launched until ten valid trajectories were obtained under nominally identical conditions to reduce the impact of anomalies such as variations in the launch sequence. The launch system was tuned to achieve a mean Reynolds number of 9.34×10^3 based on the MAC. The measured trajectories were then used to compare glide angle and $\left(\frac{L}{D}\right)_{\text{eff}}$ between configurations.

2.3 Data Processing and Glide Ratio Calculation

VICON recordings were trimmed so that Frame 1 corresponded to take-off. The trajectories were smoothed using a Savitzky-Golay (SG) filter (order 3, frame 11). Per-frame means of X, Y, Z were found, and initial speeds at t_0 were calculated with a forward difference. With the MAC and dynamic viscosity (μ), the Reynolds number was calculated for each test. For visualisation, the trajectories for each configuration were length-aligned: the longest run set the target length, and shorter runs were padded with their landing coordinate to enable frame-wise averaging, shown in Figures 5 and 6.

For each valid launch, the glide angle was calculated using the endpoint displacement over the flight window (Eq. 3). The tracked window for this calculation was between the launch altitude and 0.5 m above the ground. $\left(\frac{L}{D}\right)_{\text{eff}}$ was calculated as the cotangent of the glide path angle [23] (Eq. 4).

$$d_H = \sqrt{(\Delta X)^2 + (\Delta Y)^2} \tag{2}$$

$$\theta = \arctan\left(\frac{|\Delta Z|}{d_H}\right) \tag{3}$$

$$\left(\frac{L}{D}\right)_{\text{eff}} = \frac{d_H}{|\Delta Z|} = \cot\theta \tag{4}$$

A Reynolds number repeatability check was performed using a $\pm 2\sigma$ criterion about the overall mean. Any configuration with a mean Reynolds number outside this range was retested. For each model r, the mean glide path angle $\bar{\theta}_r$, standard deviation $s_{\theta,r}$, and signal-to-noise ratio η_r were calculated from the $n_r = 10$ valid launches [24] and [25, p. 268, Eq. 12.141]:

$$\eta_r = -10 \log_{10}\left(\frac{1}{n_r}\sum_{i=1}^{n_r} |\theta_{ri}|^2\right) \tag{5}$$

where θ_{ri} is the glide angle of launch i for model r.

The grand means act as a baseline reference for each factor, and are calculated for the S/N ratio and the glide path angle. For each factor $f \in \{\text{Planform},\ \text{Corrugation Type},\ \text{Amplitude},\ \text{Location}\}$ and each of its levels ℓ (e.g. Rectangular vs. Bio-inspired, Low vs. Medium vs. High, etc.), the mean response at that level was computed. Here, R represents the response being analysed, and is taken as either the glide path angle θ or the signal-to-noise ratio η. These quantities represent the main effects, showing how the response changes when a factor is set to a given level, averaged over all other factors. Following this, the impact that each factor and level has on the response is evaluated. Eqn. (6) [25, Chap. 30, pp. 527–528, Eqs. 30.21–30.29] defines the one-way sum of squares for a factor f. This measures the extent to which the mean response at each level ℓ of factor f deviates from the grand mean response $\bar{R}$, weighted by the number of experimental runs at that level. A large value of SS_f suggests that changes in the factor levels produce substantial variation in the selected response, whereas a small value suggests that the factor has little influence.

$$SS_f = \sum_{\ell} n_{f,\ell}, \left(\bar{R}_{f,\ell} - \bar{R}\right)^2 \tag{6}$$

Eqn. (7) shows the relative contribution of factor f as a percentage of the total variation explained by all factors, allowing for direct comparison of factor importance.

$$\%_f = \left(\frac{SS_f}{\sum_{f'} SS_{f'}}\right) \times 100 \tag{7}$$

A key aspect, and limitation of the Taguchi method, is that it assumes negligible interactions between factors. Following this logic, Taguchi main-effect additivity gives the predicted glide path angle and S/N ratio for any factor combination of (P,C,A,L), referring to Planform, Corrugation Type, Amplitude, and Location respectively, using Eqs. 8a and 8b [25, Chap. 35, pp. 593–594, Eqs. 35.9–35.11]:

$$\widehat{\theta}(P,C,A,L) = \left(\bar{\theta}_P + \bar{\theta}_C + \bar{\theta}_A + \bar{\theta}_L\right) - (k-1)\bar{\theta}, \quad k = 4, \tag{8a}$$

$$\widehat{\eta}(P,C,A,L) = \left(\bar{\eta}_P + \bar{\eta}_C + \bar{\eta}_A + \bar{\eta}_L\right) - (k-1)\bar{\eta}. \tag{8b}$$

To decide on the optimal configuration, complementary criteria were used:

1. *Shallowest glide* - select the feasible combination that minimises $\widehat{\theta}(P,C,A,L)$.
2. *Robustness* - select the feasible combination that maximises $\widehat{\eta}(P,C,A,L)$.

To communicate this, all feasible (P,C,A,L) combinations are ranked by $\widehat{\theta}$ from shallowest to steepest, with ties broken by higher $\widehat{\eta}$. Smooth baseline configurations were retained for direct comparison but were not interpreted as physical amplitude or location levels.

However, it is important to highlight the limitations in the methodology used. Primarily, the L18 approach assumes weak interactions; yet an amplitude–location dependency was evident. A higher-resolution array (e.g. L36) would better determine whether the interaction exists, and reveal any additional interactions. From a manufacturing perspective, micro-roughnesses on the wings will have introduced some uncertainty in their performance, especially surrounding the models that required additional support removal. Lastly, tests were fixed at conditions around $\mathrm{Re} \sim 10^4$, with wing incidence angles of 4°. For this reason, the results are localised to these conditions. Whilst the trends may remain broadly similar under comparable conditions, there may be some variation between different flight conditions.

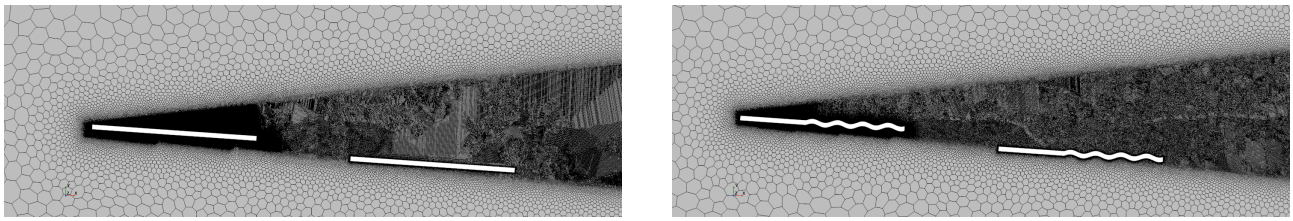
2.4 Implicit Unsteady CFD Setup

To support interpretation of the experimental trends, two-dimensional implicit unsteady CFD simulations were performed in Siemens Star-CCM+ for Model 01, the smooth rectangular baseline, and Model 05, the best-performing corrugated configuration. Both cases used the experimental

tandem-wing spacing of $1.5c$ horizontally and $0.2c$ vertically, with a geometric angle of attack of 4°. The freestream velocity was set to match the experimental Reynolds number of approximately $Re \approx 9 \times 10^3$, based on the mean aerodynamic chord.

The physics continuum used a two-dimensional, constant-density, laminar model with a coupled implicit flow solver. A laminar model was selected to resolve the coherent separated shear layers, vortex growth, and vortex shedding expected at this Reynolds number, without introducing a RANS closure that could damp or smear the vortical structures of interest. Time advancement used an implicit unsteady formulation with a timestep of $\Delta t = 8.0 \times 10^{-4}$ s. Each case was initialised to the freestream condition and simulated for $t = 0$–4 s, with aerodynamic coefficients and flow-field statistics evaluated over the full physical-time interval.

The CFD is used for mechanistic interpretation rather than full quantitative validation, since the 2D laminar formulation does not capture finite-span effects, tip vortices or spanwise instabilities present in the physical glider. The near-field meshes for the two CFD cases are shown in Figure 4.



(a) Model 01 smooth baseline mesh

(b) Model 05 corrugated mesh

Figure 4 – Near-field mesh comparison for the smooth baseline and best-performing corrugated configuration.

3. Results

3.1 Flight Test Results

A total of 214 launches were required to obtain 180 valid launches, corresponding to 10 valid launches for each of the 18 configurations. Invalid datasets mainly resulted from marker-tracking loss or inconsistent release of the launch coupler.

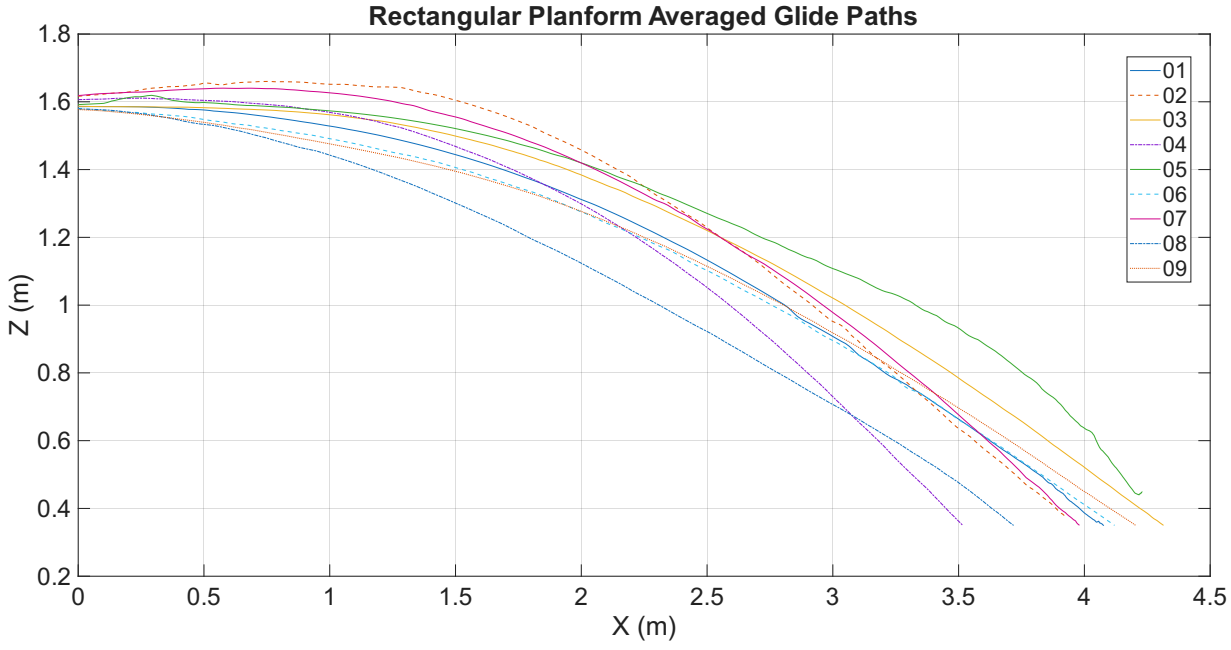


Figure 5 – Averaged glide paths for the rectangular planform configurations, shown in the vertical flight plane.

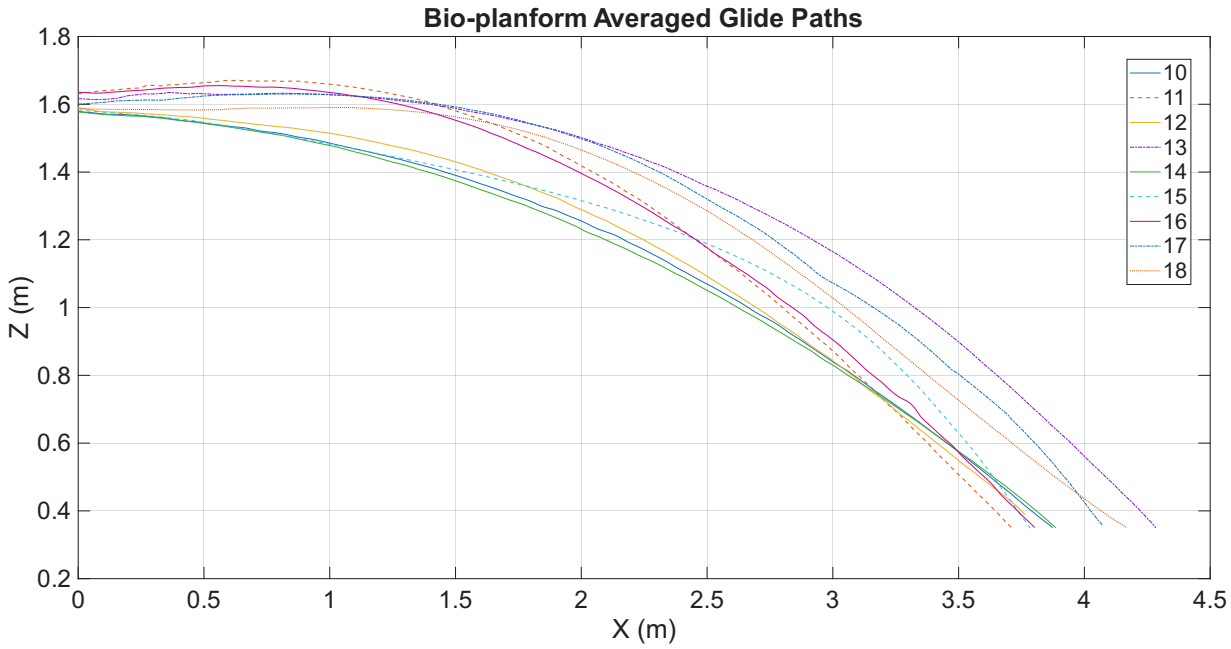
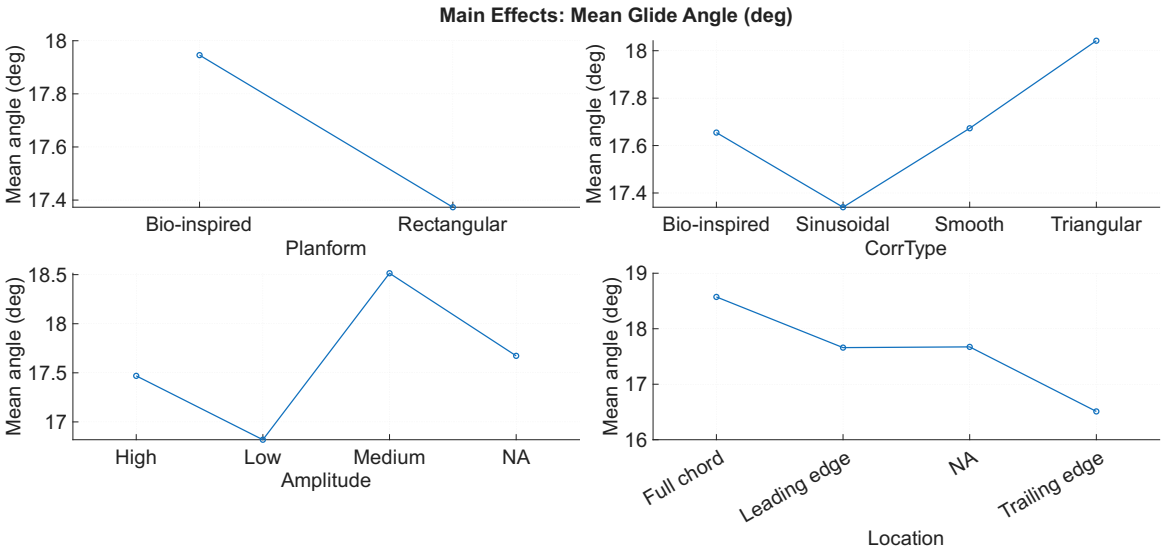


Figure 6 – Averaged glide paths for the bio-inspired planform configurations, shown in the vertical flight plane.

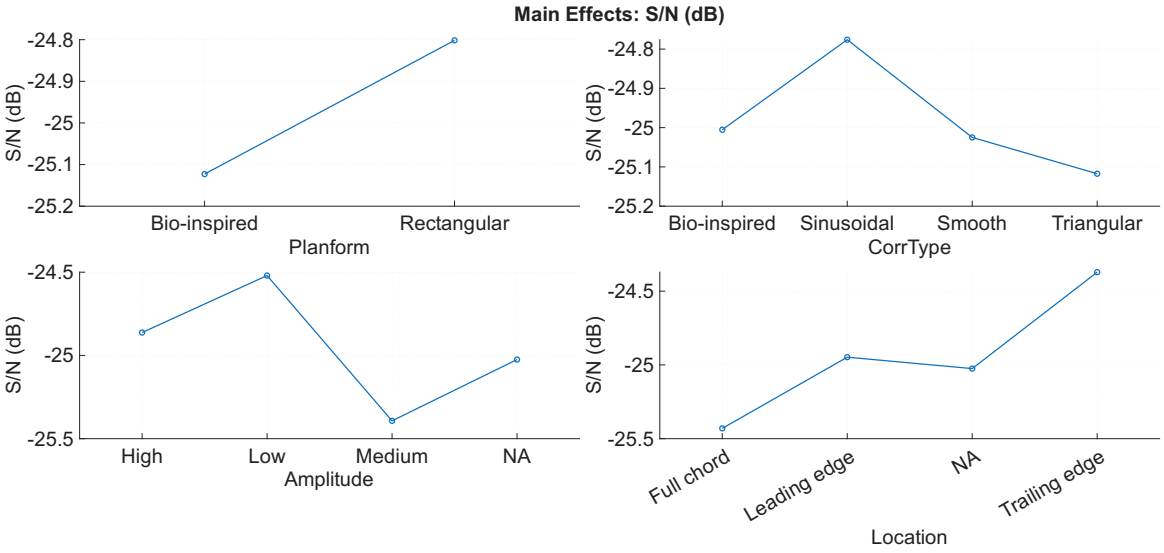
Table 7 ranks the configurations from shallowest to steepest glide path angle. Model 05 (rectangular, sinusoidal, low-amplitude, trailing-edge corrugation) achieved the best performance, increasing $\left(\frac{L}{D}\right)_{\text{eff}}$ by 17.5% relative to the smooth rectangular baseline. Main-effects plots for glide angle and S/N ratio are shown in Figure 7.

Table 7 – Glide path angles with mean Reynolds number and mean effective glide ratio for each configuration.

Model	$\overline{\text{Re}}$	θ_{glide} [°]	$\left(\frac{L}{D}\right)_{\text{eff}}$
05	9.33×10^3	14.91	3.76
03	9.42×10^3	16.19	3.44
09	9.50×10^3	16.54	3.37
18	9.08×10^3	16.63	3.35
13	9.68×10^3	16.73	3.33
06	9.24×10^3	16.96	3.28
01	9.46×10^3	17.34	3.20
02	9.21×10^3	17.61	3.15
14	9.05×10^3	17.64	3.14
15	9.33×10^3	17.64	3.15
07	9.36×10^3	18.00	3.08
10	9.31×10^3	18.01	3.08
17	9.28×10^3	18.22	3.04
12	9.14×10^3	18.24	3.03
08	9.66×10^3	18.72	2.95
16	9.32×10^3	18.91	2.92
11	9.15×10^3	19.50	2.82
04	9.56×10^3	20.09	2.73



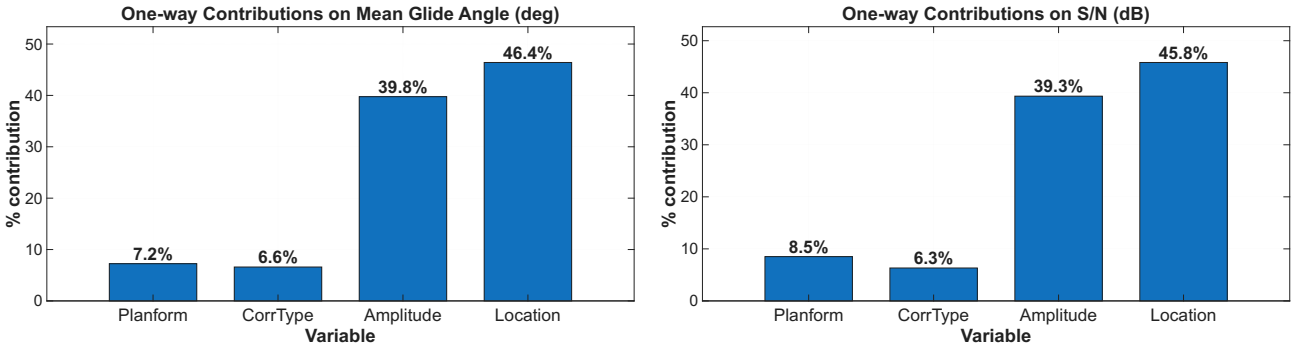
(a) Main effects plot - mean glide path angle.



(b) Main effects plot - signal-to-noise (S/N) ratio.

Figure 7 – Taguchi L18 analysis main effects plots for glide performance. (a) Mean glide path angle identifies factor levels that minimise descent steepness. (b) S/N ratio highlights factor levels that improve repeatability and reduce variability.

The glide-angle (Figure 7a) and S/N trends (Figure 7b) show the expected inverse relationship, with higher S/N generally corresponding to lower and more repeatable glide angles. The main-effects analysis identifies rectangular planform, sinusoidal corrugation, low amplitude, and trailing-edge placement as the best-performing level combination. To quantify relative importance, the following one-way contribution plots (Figures 8a and 8b) show how much each factor contributes to mean glide angle and to S/N in percentages of the total contribution. The resulting parameter ranking is summarised in Table 8.



(a) One-way contributions to mean glide path angle.

(b) One-way contributions to S/N ratio.

Figure 8 – Comparison of one-way percentage contributions for glide performance.

Table 8 – Taguchi ranking of parameters and their best-performing levels.

Rank	Parameter	Best-performing level
1	Location	Trailing edge
2	Amplitude	Low
3	Planform	Rectangular
4	Corrugation type	Sinusoidal

Additive Taguchi predictions (Figure 9) are shown as an example and were used only as screening estimates since the L18 design does not explicitly resolve factor interactions. Cells corresponding to tested configurations are marked with a red circle, and for these cases, the measured values were used directly in the predictions rather than the additive model.

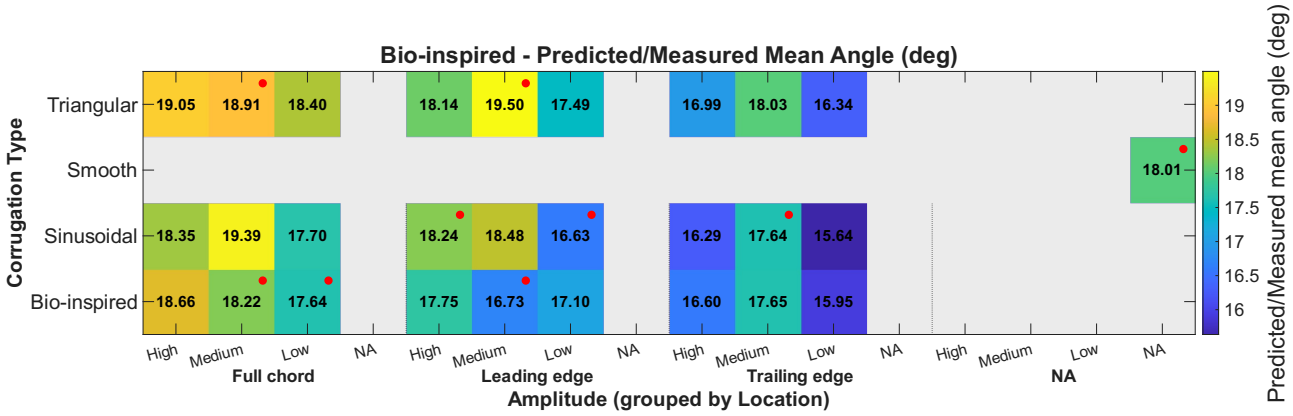


Figure 9 – Example heatmap of predicted and measured mean glide path angle (bio-inspired planform).

3.2 CFD-Based Flow-Field Interpretation

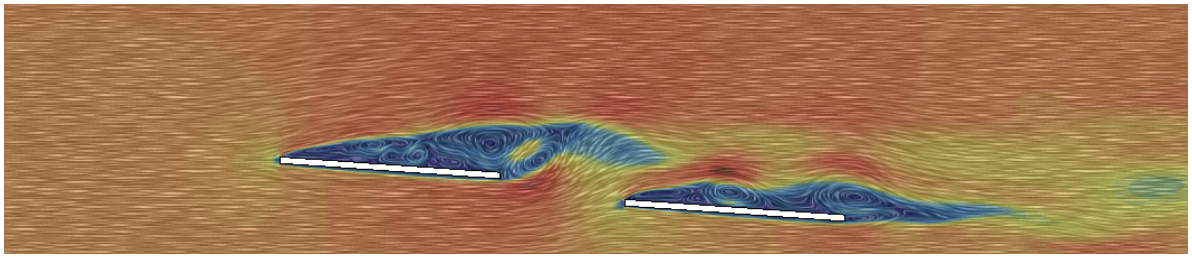
Model 05 increased experimental $\left(\frac{L}{D}\right)_{\text{eff}}$ by 17.5% relative to Model 01. The two-dimensional CFD over-predicted the absolute L/D, as expected for a model that does not capture finite-span losses, but predicted a similar relative improvement of approximately 20%. The basic numerical results between the CFD tests are summarised in Table 9, where pair-sum L/D was calculated using Eqn. 9, and the shedding frequency was obtained from the lift-coefficient time history.

$$\left(\frac{L}{D}\right)_{\text{pair}} = \frac{C_{L,\text{f}} + C_{L,\text{h}}}{C_{D,\text{f}} + C_{D,\text{h}}} \tag{9}$$

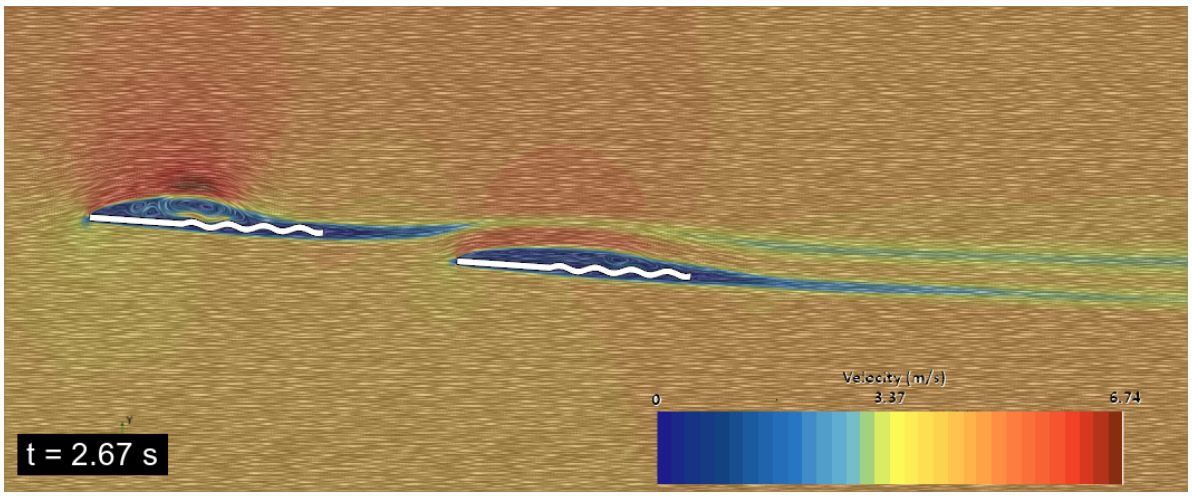
Table 9 – Force-coefficient comparison between the smooth baseline and corrugated trailing-edge configuration from implicit unsteady CFD over $t = 0$–4 s.

Quantity	**Model 01**	**Model 05**	**Change**
Forewing mean C_L	0.307	0.470	$+53\%$
Forewing mean C_D	0.068	0.071	$+4\%$
Hindwing mean C_L	0.478	0.403	-16%
Hindwing mean C_D	0.075	0.062	-19%
Pair-sum L/D	5.45	6.56	$+20\%$
Dominant shedding frequency	Aperiodic	5.6 Hz	–

The smooth baseline exhibited large-scale forewing separation, with the shed wake convecting into the hindwing and increasing hindwing separation and drag. In Model 05, trailing-edge corrugation generated valley-trapped vortices that encouraged the outer flow to bridge across the corrugation peaks, forming a pseudo-aerofoil envelope over the aft chord. This produced a narrower forewing wake and cleaner hindwing flow, consistent with the improved pair-sum L/D.



(a) Model 01 smooth baseline at $t = 2.67$ s, showing wake impingement and separated flow over the fore- and hindwing.



(b) Model 05 corrugated trailing-edge configuration at $t = 2.67$ s, showing a narrower forewing wake and cleaner hindwing flow.

Figure 10 – Instantaneous flow velocity comparison at $t = 2.67$ s. The smooth baseline exhibits a broader disturbed wake and stronger hindwing separation, whereas the corrugated trailing-edge case shows a cleaner hindwing environment and narrower wake.

The CFD suggests that Model 05 benefits from coupled forewing and hindwing effects: increased forewing lift with limited drag penalty, and a narrower forewing wake that reduces hindwing drag. This supports the experimental result that trailing-edge, low-amplitude corrugation is favourable, since it promotes vortex trapping in the aft-chord region without excessive form drag. These results remain mechanistic rather than fully validating, since the two-dimensional laminar model does not capture finite-span effects, tip vortices, spanwise instabilities, or transition.

4. Discussion

Corrugation location was the most influential parameter (Figure 8). Trailing-edge placement produced the lowest $\bar{\theta}$, whereas leading-edge and smooth configurations gave intermediate results, and full-chord corrugation performed worst overall (Figure 7a). This agrees with previous studies showing that trailing-edge corrugation can increase the pressure difference between the upper and lower surfaces, while leading-edge corrugation can reduce it. The poor performance of full-chord corrugation is likely due to repeated surface disturbances across both favourable and adverse pressure gradient regions, increasing form drag and preventing the cleaner pseudo-aerofoil behaviour associated with trailing-edge placement. This interpretation is supported by the CFD flow fields in Section 3.2, where the trailing-edge corrugated model sustained valley-trapped vortices and a cleaner aft-chord flow structure.

Corrugation amplitude was the second most influential factor, contributing roughly 40% to the variation in $\bar{\theta}$ (Figure 8). Low amplitude gave the lowest average $\bar{\theta}$, consistent with literature showing that reduced corrugation amplitude can improve aerodynamic performance by preserving the virtual surface while limiting separation and wake growth [26]. However, the non-monotonic trend observed here, with medium amplitude performing worse than both low and high amplitude, suggests that amplitude is strongly coupled to other variables, particularly corrugation location. Amplitude should therefore be treated as a tuning parameter rather than as a level that can be selected independently.

Planform shape contributed less than 10% to the variation in $\bar{\theta}$ (Figure 8). Rectangular wings gave slightly lower $\bar{\theta}$ than the bio-inspired planform, but the difference was modest because both planforms were matched in area, MAC, and thickness (Table 5). The improved rectangular performance may be linked to constant chord length, which produces a more uniform forewing wake and thus more consistent interaction with the hindwing. By contrast, the tapered bio-inspired planform introduces spanwise variation in local Reynolds number and local spacing, which may produce less uniform tandem-wing interaction. Corrugation type was the least influential of the four parameters (Figure 8), contributing less than 10% to the variation in $\bar{\theta}$. Nevertheless, a clear ordering emerges: sinusoidal corrugation yields the lowest $\bar{\theta}$ and the highest S/N ratio (Figures 7a and 7b), followed by the bio-inspired pattern, then the smooth baselines, with triangular corrugation consistently performing the worst.

The influence of corrugation type depends on how each geometry interacts with the near-surface flow and the formed boundary layer. The bio-inspired pattern, though triangular in form, tapers towards the TE, reducing the effects of separation. Smooth (uncorrugated) configurations lack these stabilising effects but also avoid the penalties of sharp peaks, placing them in the middle in terms of performance. Regular triangular corrugation is the most disruptive, with sharp uniform peaks that shed unsteady vortices into the wake, increasing drag and producing the steepest $\bar{\theta}$. This finding is consistent with prior studies, where rounded initial peaks helped to reduce near-surface rapid velocity variations and their associated drag penalties [27]. Overall, the main trends and optimal levels observed in this study are consistent with previous literature, either through direct comparison or through studies examining related corrugation parameters. Given this, it is now possible to discuss the design implications of these findings on MAV design.

The experimental 17.5% improvement in $\left(\frac{L}{D}\right)_{\text{eff}}$ is consistent with the implicit unsteady CFD prediction of approximately 20% (Section 3.2). The small difference is expected given that the free-flight experiment includes finite-span effects, trim effects, manufacturing imperfections, and tandem-wing interactions that are not fully represented in the two-dimensional simulation. Prior 2D single-wing CFD studies report larger gains (e.g. 32% [8]), consistent with the expectation that 3D effects and tandem-wing interference reduce the net benefit in realistic configurations.

An important aspect of the results is that these conclusions were obtained using a tandem-wing setup, rather than a single wing. The corrugation location, amplitude, and waveform trends are expected to be largely transferable to single-wing setups given that the mechanisms are governed by

the local low-Reynolds flow properties. However, the magnitude of the improvement, particularly for the planform trend, should not be assumed to transfer directly to a single-wing case. A corrugation pattern that narrows the forewing wake has a substantial impact on the performance of the hindwing flow environment, thus changing the corrugation-driven mechanisms on the hindwing. Consequently, the obtained results are best interpreted as design guidance for tandem-wing MAVs, with the local corrugation results likely to remain useful for single-wing MAVs, but requiring further validation.

Within the $Re \sim 10^4$ envelope tested here, the recommended baseline is a rectangular planform with low-amplitude sinusoidal corrugation confined to the trailing-edge region, $0.4 \leq x/c \leq 1.0$. If a higher amplitude is needed for structural reasons, it should be applied only at the TE; the same increase elsewhere raises $\bar{\theta}$ and negates the aerodynamic benefit. If a purely sinusoidal waveform is not feasible, a bio-inspired (tapered triangular) pattern is preferable to a regular triangular pattern, and amplitude should remain low. Full-chord corrugations should be avoided because they exacerbate the penalties of LE corrugation. The implicit unsteady flow fields in Section 3.2 support this guidance directly: the pseudo-aerofoil mechanism is active in the TE region where trapped valley vortices sustain a smooth effective upper-surface contour (Figure 10b), and the resulting narrow forewing wake reduces unsteady wake forcing on the hindwing.

5. Conclusions

This study showed that low-amplitude sinusoidal corrugation applied at the trailing edge of a rectangular wing produced the greatest aerodynamic performance for a tandem-wing MAV glider within the tested $Re \sim 10^4$ envelope, improving $\left(\frac{L}{D}\right)_{\text{eff}}$ by approximately 17.5% relative to a smooth rectangular baseline. Corrugation location was found to be the dominant parameter, followed by amplitude, whilst corrugation type and wing planform had smaller, broadly comparable influences. Targeted implicit unsteady 2D CFD simulations predicted a comparable relative improvement of approximately 20%, supporting the proposed flow-mechanism interpretation. The simulations indicated that the performance improvement was associated with valley-trapped vortices, pseudo-aerofoil formation, and a narrower wake structure.

The conclusions are specific to the tested geometry, Reynolds number, wing incidence angle, and tandem-wing arrangement. Nevertheless, these results may still be relevant to similar-scale MAV concepts, although further validation and envelope expansion are required. Future work should therefore act to expand the design space to resolve interaction effects, compare the corrugated configurations against conventional aerofoil baselines (e.g. NACA sections), and assess how the trends change for single-wing configurations, different Reynolds numbers, and wider angle-of-attack ranges.

Ultimately, these findings provide practical design guidance for improving the aerodynamic efficiency of MAV-scale gliders operating in low-Re regimes, particularly where passive geometric flow-control features can help to extend range and endurance. More broadly, the results provide an experimental contribution to the understanding of tandem-wing gliding and complement previous studies of corrugated aerofoils by validating similar performance-enhancing mechanisms in free-flight MAV conditions.

6. Contact Author Email Address

The contact author email address is: melos_krasniqi@outlook.com.

7. Copyright Statement

The authors confirm that they, and/or their company or organization, hold copyright on all of the original material included in this paper. The authors also confirm that they have obtained permission, from the copyright holder of any third party material included in this paper, to publish it as part of their paper. The authors confirm that they give permission, or have obtained permission from the copyright holder of this paper, for the publication and distribution of this paper as part of the ICAS proceedings or as individual off-prints from the proceedings.

References

[1] Yang Z and Hu H. Laminar flow separation and transition on a low-Reynolds-number airfoil. *Journal of Aircraft*, Vol. 45, pp. 1067–1070, 2008. https://doi.org/10.2514/1.35051.

[2] Winslow J, Otsuka H, Govindarajan B, and Chopra I. Basic understanding of airfoil characteristics at low Reynolds numbers (10^4–10^5). *Journal of Aircraft*, Vol. 55, No. 3, pp. 1050–1061, 2018. https://doi.org/10.2514/1.C034415.

[3] Yu M, Hrynuk J T, Booth D T, and Poudel N. Freestream turbulence effects on low Reynolds number NACA 0012 airfoil laminar separation bubble and lift generation. *Aerospace Science and Technology*, Vol. 149, p. 109145, 2024. https://doi.org/10.1016/j.ast.2024.109145.

[4] Chen Y and Skote M. Gliding performance of 3-D corrugated dragonfly wing with spanwise variation. *Journal of Fluids and Structures*, Vol. 62, pp. 1–13, 2016. https://doi.org/10.1016/j.jfluidstructs.2015.12.012, URL https://www.sciencedirect.com/science/article/pii/S0889974616000098.

[5] Jongerius S R and Lentink D. Structural analysis of a dragonfly wing. *Experimental Mechanics*, Vol. 50, No. 9, pp. 1323–1334, 2010. https://doi.org/10.1007/s11340-010-9411-x.

[6] Lurans E, Alhinai A, and Viswanathan H. Aerodynamics of corrugated wings: past, present, and future. *Aerospace*, Vol. 12, No. 3, p. 262, 2025. https://doi.org/10.3390/aerospace12030262.

[7] Lamb G, Magesh A, Mahavratayajula A, Pechiammal A, Bhargava D, Holloway J, and Miramontes A. A CFD investigation of dragonfly flight: aerodynamic analysis of corrugated wings using static and dynamic meshing in OpenFOAM. *2025 Regional Student Conferences*, American Institute of Aeronautics and Astronautics, 2025. https://doi.org/10.2514/6.2025-98862.

[8] Vargas A, Mittal R, and Dong H. A computational study of the aerodynamic performance of a dragonfly wing section in gliding flight. *Bioinspiration & Biomimetics*, Vol. 3, No. 2, p. 026004, 2008. https://doi.org/10.1088/1748-3182/3/2/026004.

[9] Narita Y and Chiba K. Aerodynamics on a faithful hindwing model of a migratory dragonfly based on 3D scan data. *Journal of Fluids and Structures*, Vol. 125, p. 104080, 2024. https://doi.org/10.1016/j.jfluidstructs.2024.104080, URL https://www.sciencedirect.com/science/article/pii/S088997462400015X.

[10] Kesel A B. Aerodynamic characteristics of dragonfly wing sections compared with technical aerofoils. *Journal of Experimental Biology*, Vol. 203, No. 20, pp. 3125–3135, 2000. https://doi.org/10.1242/jeb.203.20.3125.

[11] Okamoto M, Yasuda K, and Azuma A. Aerodynamic characteristics of the wings and body of a dragonfly. *Journal of Experimental Biology*, Vol. 199, No. 2, pp. 281–294, 1996. https://doi.org/10.1242/jeb.199.2.281.

[12] Tamai M, Wang Z, Rajagopalan G, Hu H, and He G. Aerodynamic performance of a corrugated dragonfly airfoil compared with smooth airfoils at low Reynolds numbers. *45th AIAA Aerospace Sciences Meeting and Exhibit*, American Institute of Aeronautics and Astronautics, 2007. https://doi.org/10.2514/6.2007-483.

[13] Obata A and Sinohara S. Flow visualization study of the aerodynamics of modeled dragonfly wings. *AIAA Journal*, Vol. 47, No. 12, pp. 3043–3046, 2009. https://doi.org/10.2514/1.43836.

[14] Huang M and Wang Z w. A review of wind tunnel based virtual flight testing techniques for evaluation of flight control systems. *International Journal of Aerospace Engineering*, Vol. 2015, No. 1, p. 672423, 2015. https://doi.org/10.1155/2015/672423.

[15] Meng X and Sun M. Aerodynamic effects of corrugation in flapping insect wings in forward flight. *Journal of Bionic Engineering*, Vol. 8, No. 2, pp. 140–150, 2011. https://doi.org/10.1016/S1672-6529(11)60015-2, URL https://www.sciencedirect.com/science/article/pii/S1672652911600152.

[16] Au L T K, Phan H V, Park S H, and Park H C. Effect of corrugation on the aerodynamic performance of three-dimensional flapping wings. *Aerospace Science and Technology*, Vol. 105, p. 106041, 2020.

[17] Meng X G and Sun M. Aerodynamic effects of wing corrugation at gliding flight at low Reynolds numbers. *Physics of Fluids*, Vol. 25, No. 7, p. 071905, 2013. https://doi.org/10.1063/1.4813804.

[18] NCSS Statistical Software. *Taguchi designs*, NCSS, LLC, 2025. URL https://www.ncss.com/wp-content/themes/ncss/pdf/Procedures/NCSS/Taguchi_Designs.pdf, chapter 266 in NCSS Documentation.

[19] Department of Mathematics, University of York. Orthogonal arrays (Taguchi designs). https://www.york.ac.uk/depts/maths/tables/orthogonal.htm, 2004. Accessed: 2025-08-23.

[20] Crowther R. Dorsal view of *Petalura ingentissima*, Tillyard, 1908 (lectotype). https://commons.wikimedia.org/wiki/File:013323996_Petalura_ingentissima_dorsal.jpg, Mar 2018. Photo by Robyn Crowther; Natural History Museum, London. Licensed under CC BY 4.0.

[21] Zhang J and Lu X Y. Aerodynamic performance due to forewing and hindwing interaction in gliding dragonfly flight. *Phys. Rev. E*, Vol. 80, p. 017302, 2009. https://doi.org/10.1103/PhysRevE.80.017302.

[22] Imperial College London, Department of Aeronautics. Aerial Robotics Facilities. https://www.imperial.ac.uk/aeronautics/research/facilities/aerial-robotics/, 2025. Accessed: 2025-08-28.

[23] NASA Glenn Research Center. Lift-to-drag ratio. https://www1.grc.nasa.gov/beginners-guide-to-aeronautics/lift-to-drag-ratio/, 2023. Accessed: 2025-08-29.

[24] Phadke M S. *Quality engineering using robust design*, Prentice Hall PTR, 1995.

[25] Taguchi G, Chowdhury S, and Wu Y. *Taguchi's quality engineering handbook*, Wiley, Hoboken, NJ, 2005.

[26] Zhang Z, Yin Y, Zhong Z, and Zhao H. Aerodynamic performance of dragonfly wing with well-designed corrugated section in gliding flight. *Computer Modeling in Engineering & Sciences*, Vol. 109-110, No. 3, pp. 285–302, 2015. https://doi.org/10.3970/cmes.2015.109.285, URL http://www.techscience.com/CMES/v109-110n3/27301.

[27] Dwivedi Y D and Bhargava Nukala V. Aerodynamic characterization of bio inspired corrugated wings. *Applied Bionics and Biomechanics*, Vol. 3, pp. 1–10, 2019. https://doi.org/10.15406/mojabb.2019.03.00092.